Article

Quasi-equilibrium, multi-foil platelets of copper and titanium substituted bismuth vanadate, $Bi_2V_{0.9}(Cu_{0.1-x}Ti_x)O_{5.5-\delta}$, by molten salt synthesis

Kevin Ring[1], Paul Fuierer[1*]

[1] Materials and Metallurgical Engineering Department, New Mexico Institute of Mining and Technology (New Mexico Tech), 801 LeRoy Place, Socorro NM 87801

* Corresponding Author: paul.fuierer@nmt.edu ; Tel.: +01-575-835-5497

Abstract: 10% copper substituted (BiCUVOX/$Bi_2V_{0.9}Cu_{0.1}O_{5.5-\delta}$) and 5% copper/titanium double-substituted bismuth vanadate (BiCUTIVOX/$Bi_2V_{0.9}(Cu_{0.05}Ti_{0.05})O_{5.5-\delta}$) platelets were formed by molten salt synthesis (MSS) using a eutectic KCl/NaCl salt mixture. The product was phase pure within the limits of x-ray diffraction. The size and form of the platelets could be controlled by changing the heating temperature and time. The crystallite growth rate at a synthesis temperature of 650°C, and activation energy for grain growth were determined for BICUTIVOX, which experienced inhibited growth compared to BICUVOX. Quasi-equilibrium, multi-foil shapes consisting of lobes around the perimeter of the platelets were observed and explained in the context of relative two-dimensional nucleation and edge growth rates.

Keywords: Bismuth vanadate, molten salt synthesis, platelet morphology, multi-foil shape, Wulff shape, Ostwald ripening

1. Introduction

In 1988 Abraham et al published the discovery of a new group of oxide ion conducting ceramics based on bismuth vanadate ($Bi_4V_2O_{11-\delta}$) [1]. This compound was determined to be a member of the Aurivillius family of crystal structures, and was described as having alternating layers of $(Bi_2O_2)^{2+}$ and $(VO_{3.5}\square_{0.5})^{2-}$ [1]. Bismuth vanadate has three distinct phases, and from single crystal studies the highest temperature γ-phase (normally occurring at T>550°C) was determined to be tetragonal (space group *I4/mmm*, *a*=4.004 Å, *c*=15.488 Å). Conductivity was found to be highly anisotropic; 2 orders of magnitude higher perpendicular to the c-axis (in the *a-b* plane) than parallel to the *c* axis [1-4]. It was later found that partial substitution of an aliovalent metal cation for vanadium (first was copper at 10 mol %) resulted in the stabilization of the γ-phase at room temperature, and the term BIMEVOX was coined to refer to this and all subsequent formulations, where ME represents one of many possible substitutive metal cations, typically a transition metal [2]. Having higher oxide ion conductivity higher than any other ceramic (e.g. yttria-stabilized cubic zirconia ($Zr_{1-x}Y_xO_{2-x/2}$ "YSZ") at moderate temperatures, BIMEVOX compounds have generated interest over the years for potential applications including solid-oxide fuel cells, oxygen separation pumps, gas sensors [5-9], and very recently as catalyst supports [10].

Just as with its conductivity, the anisotropy of the tetragonal phase is expected to result in anisotropy in other chemical and physical tensor properties of BIMEVOX. While such differences are distinct in single crystals, a random polycrystalline sample exhibits an approximate average of

Peer-reviewed version available at Crystals 2018, 8, 170; doi:10.3390/cryst8040170

the lattice-specific property coefficients. Enhancing long range texture of polycrystalline samples therefore holds promise for enhancing the desired properties of BIMEVOX ceramics; of chief interest is maximizing the bi-dimensional ionic conductivity [11]. Experimental techniques for enhancing the texture of anisotropic ceramics have included pulsed laser deposition [12], magnetic or electric fields [13, 14], and load-assisted sintering or "hot-forging" [14-16]. Shantha *et al.* [17], used a KCl flux in a two-stage, liquid phase sintering process which resulted in densities of 97% and textures up to 79% in BIMEVOX.

Another route for fabricating textured ceramics begins with particles already exhibiting the desired geometry and uses them as seeds in "templated grain growth" (TGG). TGG has been used with reasonable success in conjunction with tape-casting for bismuth titanate ($Bi_4Ti_3O_{12}$) and other layered-perovskite type compounds, achieving *(00l)* textures exceeding 90% [18-23]. Due to the crystallographic anisotropy of bismuth titanate and other Aurivillius phases, the surface energy of the *(00l)* planes is less than that of *(hk0)* planes, and therefore the growth of anisometric particles (i.e. platelets) is thermodynamically favorable; however, the kinetics in conventional, solid state synthesis often limit such growth.

Molten salt synthesis (MSS) is a favored method for producing such seed particles with pronounced anisotropic growth by reacting the material in a molten salt flux [24-29]. The molten salt acts as a diffusion enhancing medium. Phase formation occurs by one of two mechanisms, solution-precipitation or solution-diffusion, depending on the relative solubility of the reactant species [27]. Grain growth by Ostwald ripening of crystallites is controlled by 2-dimension (2D) nucleation and growth along a crystallographic vector by generation of ledges on the propagating edge [27, 30]. MSS, also called salt melt synthesis, has been used since the 1970s to synthesize binary and complex oxides using a variety of salt systems [24-27], but is getting renewed attention for producing borides, carbides, silicides and nanomaterials with high crystallinity [28, 29]. MSS is high temperature solution chemistry, but, compared to solid state synthesis, allows lower reaction temperatures and much faster mass transport by means of convection and diffusion through the liquid phase. The process is also attractive because it can be scaled up and, depending on the salt system used, can be economical and environmentally friendly with recycling of water-soluble salts.

Roy and Fuierer [31] first published work on the successful synthesis of BICOVOX (cobalt-substituted bismuth vanadate) by MSS. Herein, we report for the first time the molten salt synthesis of BICUVOX or BICUTIVOX using similar techniques. The hypothesis is that the product of the solubility of oxide constituents, $[Bi_2O_3]^2[V_2O_5]^{1-x-y}[CuO]^x[TiO_2]^y$, is larger than the solubility of $Bi_4(V_{1-x-y}Cu_xTi_y)_2O_{11-\delta}$, leading to its formation under a high degree of supersaturation. Subsequent grain growth is expected to lead to highly anisometric particles.

2. Materials and Methods

Stoichiometric amounts of bismuth (III) oxide (Alfa Aesar, 99%), vanadium (V) oxide (Acros Organics 99.6+%), titanium (IV) oxide (JT Baker, ACS grade), and copper (II) oxide (Aldrich, ACS grade) were combined with an equal mass of a eutectic (T_E=640-657°C [32]) salt mixture: 0.506:0.494 molar ratio of sodium chloride (Fisher, 99+%) and potassium chloride (Aldrich 99+%). The batches were milled in a 250 mL, HDPE jar with 400 grams of 13 mm cylindrical, ceria-stabilized zirconia media, at approximately 130 rpm typically for 5 hours. Milling was performed dry, the media and powder were separated after milling using a #10 sieve. Reactions were carried out in air, using a

Thermolyne 47900, resistive wire heated muffle furnace. The material was placed in a covered alumina crucible and heated at a ramp rate of 10°C/min to temperatures between 610°C and 700°C, and held for 2 to 10 hours. Net loss of mass after heat treatments never exceeded 0.5%. After heating, the charge of product and fused salt was broken up by soaking in deionized water at ~75°C and then splitting to expose the interior. The aggregated material was broken up and washed of salt by stirring in 1.4 L of DI H_2O at 60°C for periods of 30 minutes to 18 hours. After the material settled, the water was decanted and replaced. This process was repeated a minimum of four times. The final product was oven dried.

Powder samples for analysis were taken by stirring the entire yielded quantity and taking material from the center. XRD analysis was carried out with a PANalytical X'Pert Pro ($Cu_{K\alpha}$ source, nickel filter, and a 2.122° X'Celerator line detector) over a 2θ of 5.996° to 70°, with 0.01671° steps, and the data was analyzed with the accompanying HiScore Plus software. Data presented were modified from the raw scan data by dividing the intensity at each 2θ value in a set by the maximum intensity in that set (*i.e.*, normalized to 1) and then patterns were shifted by integer values to accommodate multiple patterns on the same chart. All patterns were indexed as *I*4/*mmm* tetragonal, according to ICCD PDF #01-070-9191 [33]. Microscopic analysis was performed using an Hitachi S-3200N scanning electron (SE) microscope. Crystallite platelet dimensions were measured using image digitization of SE micrographs. Particle size distribution analysis was performed by Fraunhoffer laser (780 nm) diffraction using a Beckman Coulter LS 13 3220 with the micro liquid module filled with deionized water and loaded to 8-12% obscuration.

3. Results and Discussion

The series of XRD patterns for BICUVOX in Figure 1 shows that the γ-phase was successfully synthesized at all heat treatments and that no other phases were present within detectable limits. The enhanced ratio of *(00l)/(013)* peak intensities compared to the random powder pattern peak heights is an indication of an increase in population of *c*-axis oriented platelets and their alignment under the mild shearing forces involved in the preparation of a powder sample for XRD analysis [34]. Comparing different temperatures, the sample synthesized at 650°C shows higher intensity *(00l)* reflections than the material synthesized at 610°C and at 675°C. For the purposes of strong crystallite texturing, the result suggests that 650°C is the best synthesis temperature.

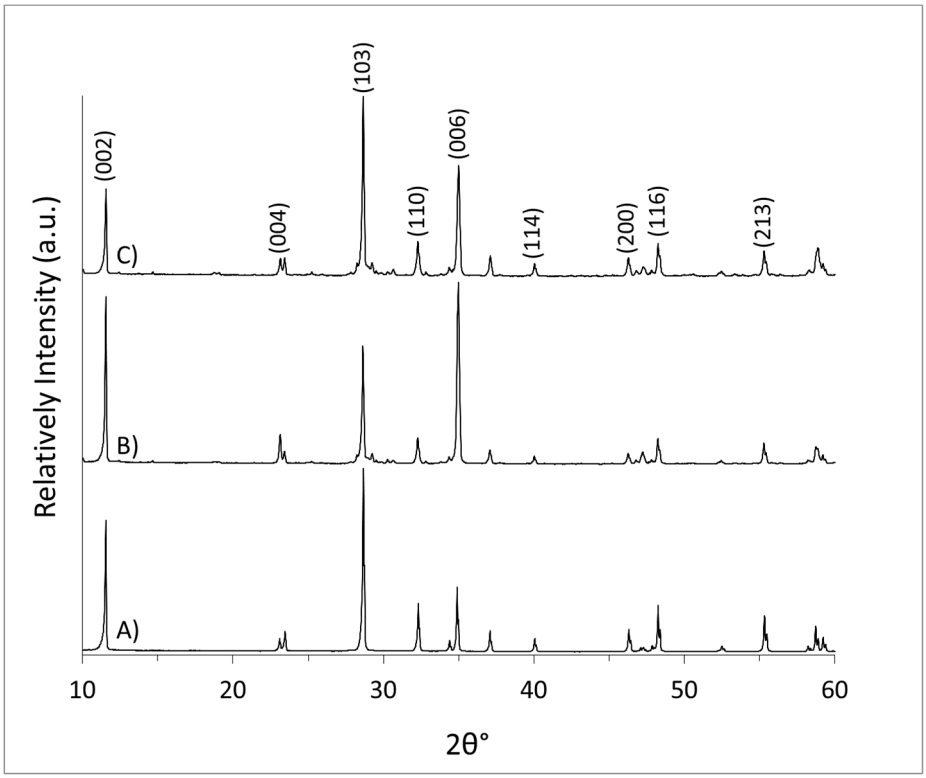

Figure 1. XRD pattern of BICUVOX platelets synthesized by MSS: A) 610°C/8hr, B) 650°C/8hr, C) 675°C/8hr.

Error! Reference source not found. shows SEM images of MSS BICUVOX. The 610/8 material appears to consist largely of agglomerates of small platelets. Although 610°C is substantially lower than the reported eutectic temperature of 640-657°C [32], the solid salt still facilitates habit growth by enhancing the diffusion of ions [35]. With higher process temperatures and presence of molten salt, larger platelets result, with a majority of the faces having an irregular shape. Inspection of additional micrographs suggests that the highest temperature (675°C) also gives a greater population of smaller crystallites, resulting either from fracture or larger platelets dissolving and re-nucleating as described in [26,30,31]. An increase in population of broken and/or re-dissolved and nucleated particles is believed to be the cause of the decrease in *(00l)* reflections for the 675°C processed material. Figure 3 shows the distribution of particle sizes as measured by laser diffraction. As expected, the major mode shifts to larger particle size with process temperature and time, in general agreement with the SEM images. For the solid-salt synthesis at 610°C, the small mode at large size of about 80 microns is attributed to aggregation. For the 675°C material, the shoulder located at about 30 µm off of the major peak can be attributed to broken platelets.

132

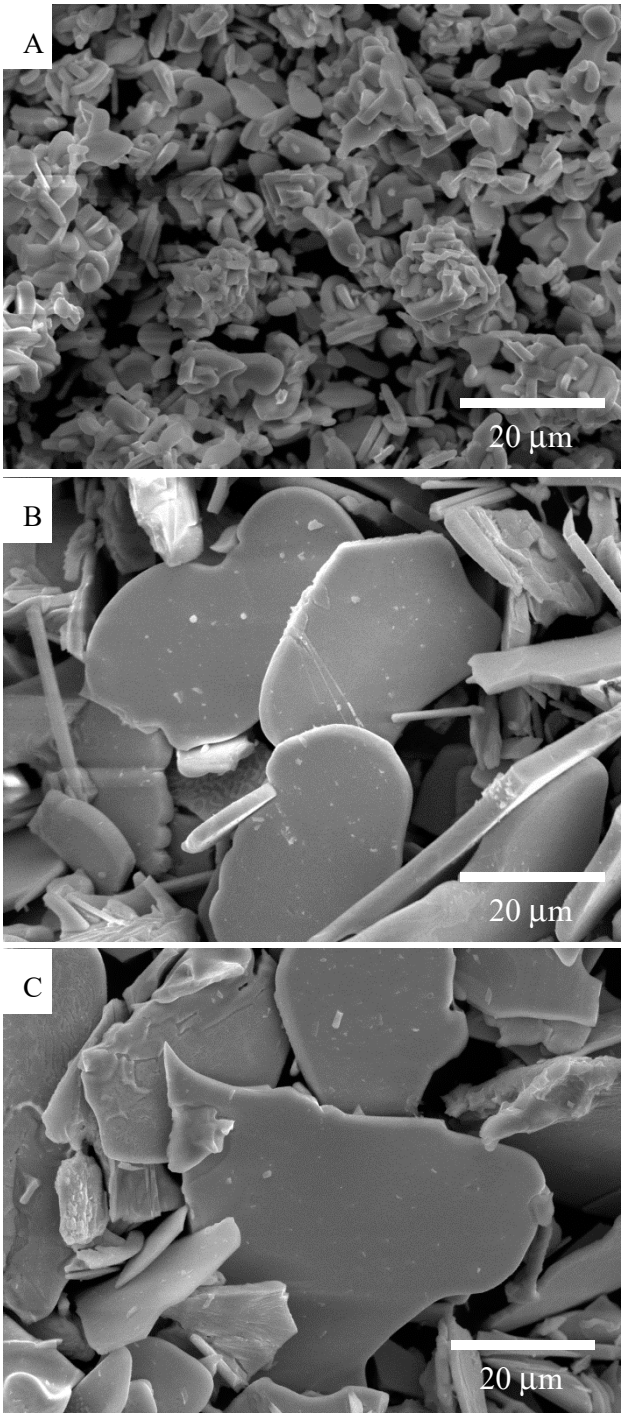

133

134 **Figure 2.** SEM images of BICUVOX platelets formed by MSS at: A) 610°C/8hr, B) 650°C/8hr, C) 675°C/8hr.

135

136

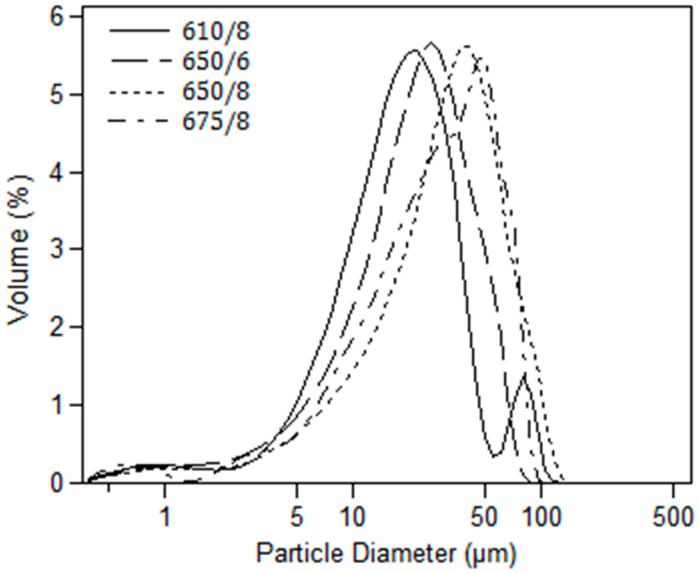

Figure 3. Relative volume distribution of particle sizes for BICUVOX powders synthesized using salt matrix at various treatment temperatures.

The diffraction patterns in Figure 4 show that the γ-phase for BICUTIVOX was also synthesized at all heat treatments. All three patterns again show higher *(00l) / (103)* intensity ratios than a random powder pattern [33]. In this case, there is a steady decrease in powder texture with increasing synthesis temperature.

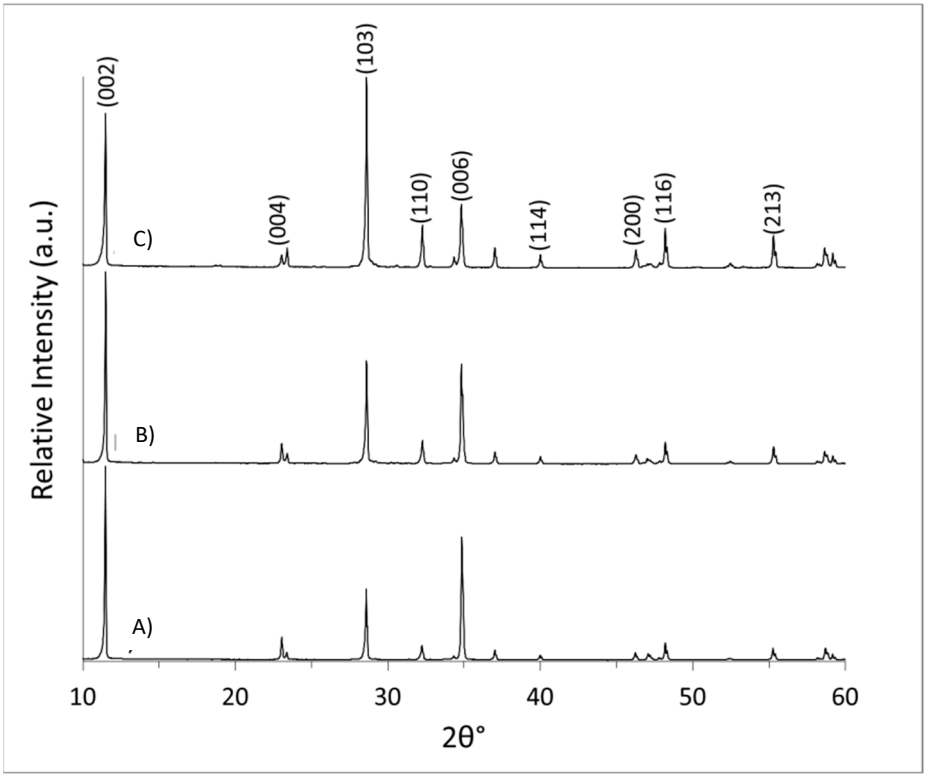

Figure 4. XRD pattern of BICUTIVOX platelets produced via MSS: A) 650°C/8hr, B) 675°C/8hr C) 700°C/8hr.

The SEM images in Figure 5 show populations of platelets, some quite rounded, and others irregular in geometry. The occurrence of platelets with edge-lobes and multi-foil shape [36] is evident. A mechanistic explanation for the platelet shape and edge lobes is proposed later in the manuscript. The size of platelets shows a steady increase with process temperature. Figure 6 shows the size distribution of particles by laser diffraction, and shows the major peak shifting to smaller size with increasing temperature. This is counter to what is expected, opposite to the result for BICUVOX, and is not in agreement with the impression from the SEM micrographs. See Figure 7 for a larger perspective view and also a direct comparison of BICUVOX and BICUTIVOX at equivalent process conditions

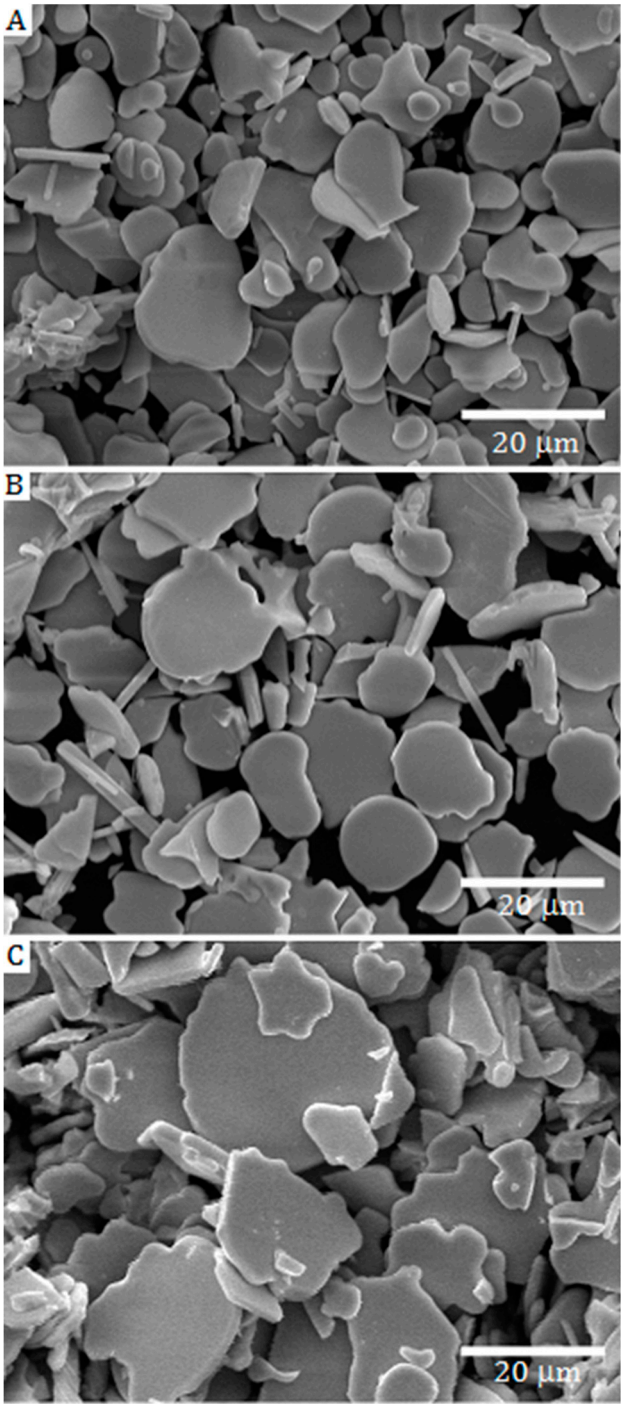

.

Figure 5. SEM images of BICUTIVOX platelets formed by MSS at: A) 650°C/8 hr, B) 675°C/8hr, C) 700°C/8hr.

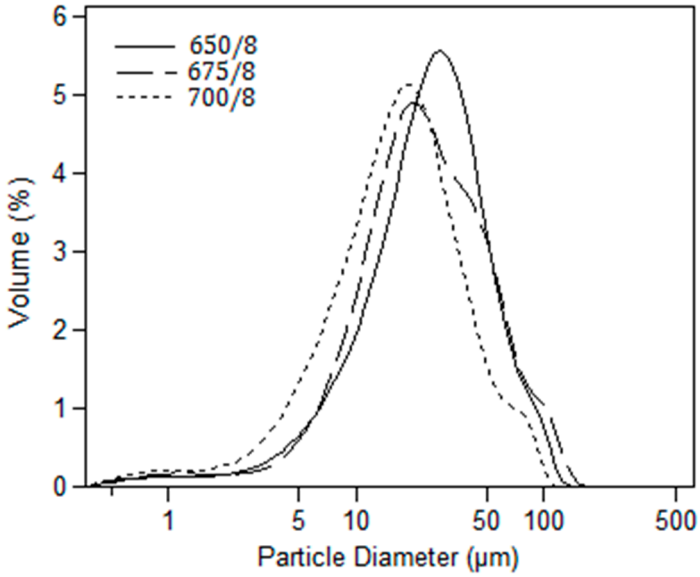

Figure 6. Relative volume particle size distribution for BICUTIVOX platelets synthesized using molten salt at various treatment temperatures.

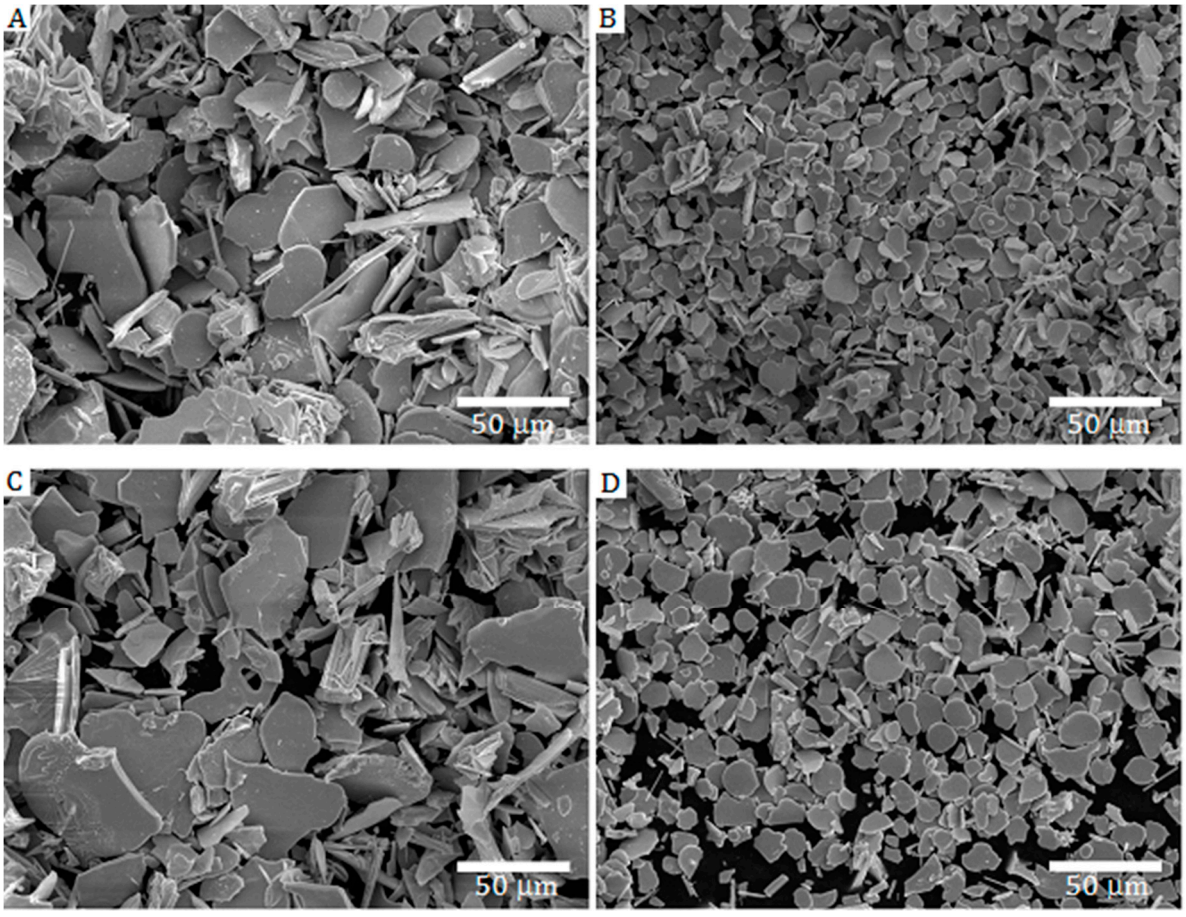

Figure 7. SEM images of BICUVOX(left) and BICUTIVOX(right) synthesized under the same conditions: A) BICUVOX, 650°C/8hr, B) BICUTIVOX, 650°C/8hr, C) BICUVOX, 675°C/8hr, D) BICUTIVOX, 675°C/8hr.

Preprints (www.preprints.org) | NOT PEER-REVIEWED | Posted: 12 March 2018 doi:10.20944/preprints201803.0082.v1

Peer-reviewed version available at Crystals 2018, 8, 170; doi:10.3390/cryst8040170

Particle sizing by laser diffraction is challenging for platelet type particles and can be misleading because the technique assumes an equivalent spherical diameter, and is subject to influences of fractured particles as well as agglomeration. So a direct approach was adopted using SEM images for more accurate particle size measurement and analytics. Four representative micrographs from each sample, with particles well dispersed on carbon tape, were carefully analyzed. Dimensions were taken of any particle with large face oriented normal to the viewing axis. Platelets which were obviously fractured were not used. Likewise, all edge-on particles were used to measure platelet thickness. Statistical values of these populations (N>100) of particles are summarized in Table 1. Despite rather large standard deviations in some samples, the table shows a general trend of increased average and maximum platelet size with increasing temperature. At a fixed process temperature of 650°C, a steady increase in average size with time is also apparent. Also given in Table 1 are Lotgering Orientation factors, *F*, obtained from the XRD patterns in Figures 1 and 4, calculated by [37]:

$$F = \frac{p-p_0}{1-p_0} \quad \text{and} \quad p = \frac{\Sigma I(00l)}{\Sigma I(hkl)} \tag{1}$$

where *p* is equal to the sum of the intensities of the selected family of planes divided by the sum of intensities for all planes within the pattern; p_0 is that factor for a non-textured sample (randomly oriented powder pattern [33]). This is a relative measure of the number and tendency for orientation of *c*-axis platelets in the packed powder XRD samples. The *F* factor is highest for a process temperature of 650°C for both materials. Platelet breakage, dissolution/nucleation and increased edge roughness are all believed to be responsible for the decrease in powder XRD texture with higher process temperature.

Table 1. Dimensional statistics and orientation factor, *F*, of salt synthesized BIMEVOX platelets.

Treatment	Phase	$F_{(00l)}$	d_{ave} ± STDEV (µm)	d_{max} (µm)	AR± STDEV
610/8	BiCuVOx	0.14	7.2 ± 1.5	11.66	8 ± 2.7
650/2	BiCuVOx		24.5 ± 2	36.3	13 ± 3
650/4	BiCuVOx		27.0 ± 4.5	47.5	13 ± 2.8
650/6	BiCuVOx	0.33	26.9 ± 7.2	35.09	12 ± 3
650/8	BiCuVOx	0.43	33.5 ± 10.3	49.35	15 ± 7.7
650/10	BiCuVOx		29.1 ± 5.5	44.88	9 ± 1.8
675/8	BiCuVOx	0.23	37.3 ± 21.1	65.53	15 ± 8.9
650/2	BiCuTiVOx		9.6 ± 0.6	12.93	8 ± 2.8
650/4	BiCuTiVOx		11.0 ± 3.2	21.70	11 ± 2.8
650/6	BiCuTiVOx		13.6 ± 0.5	18.32	9 ± 2.4
650/8	BiCuTiVOx	0.6	16.1 ± 2.7	29.22	10 ± 2.1
650/10	BiCuTiVOx		16.3 ± 3.0	24.30	7 ± 1.3
675/8	BiCuTiVOx	0.47	17.9 ± 2.8	24.96	11 ± 2.6
700/8	BiCuTiVOx	0.22	21.3 ± 4.2	32.09	10 ± 2.6

Particle growth can be represented by the following equation [38-40]:

$$D^2 - D_0^2 = k(t - t_0)\exp(-\frac{E_a}{RT}) \tag{2}$$

where D is the average particle size at time t, D_0 is the initial particle size at initial time t_0, k is the rate constant, E_a is the activation energy for particle growth, R is the gas constant, and T is the synthesis temperature. When the initial particle size, D_0, is small relative to the average D at time t, the D_0 term can be neglected. Figure 8 shows a plot of $2lnD$ vs inverse temperature for the two compositions. From the slope of the best-fit line, an activation energy of 83 kJ/mol for particle growth for BICUTIVOX is obtained. This value is between 32 kJ/mol for $BaBi_4Ti_4O_{15}$ (another Aurivilius-type phase) synthesized in K_2SO_4-Na_2SO_4 flux [40], and 96 kJ/mol for $Pb(Mg_{.33}Nb_{.67})0_3$ (perovskite) in Li_2SO_4-Na_2SO_4 flux [38], and is considered reasonably accurate. With only two molten salt data points for BICUVOX, an activation energy is not calculated, but appears to be lower than for BICUTIVOX. Also plotted on the graph is the single data point for the solid-salt synthesized BICUVOX, which falls far below the line due to a different limiting mechanism for growth in the solid state below the NaCl-KCl eutectic temperature.

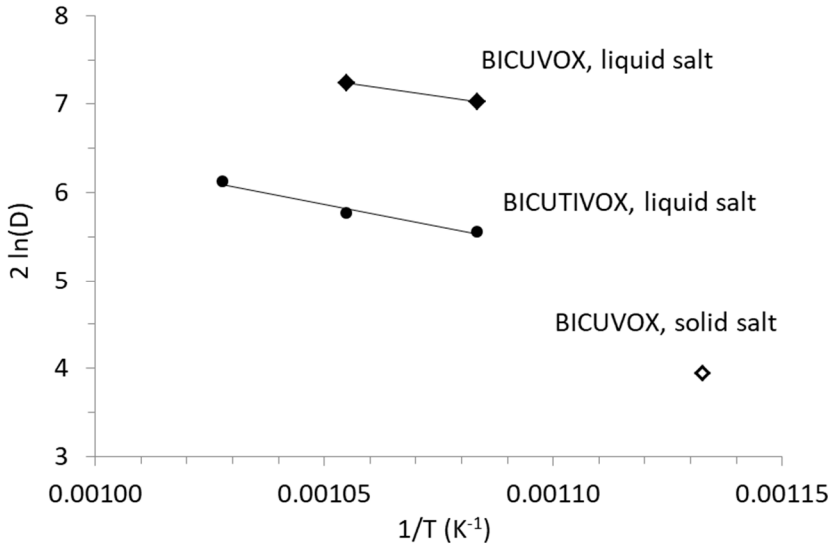

Figure 8. Plot of 2lnD (D= platelet diameter) versus inverse temperature for salt-synthesized BICUVOX and BICUTIVOX according to the particle growth model.

Also according to equation 2 and the well-known parabolic rate law, the platelet diameter, D, is plotted versus the square root of time for a process temperature of 650°C (Figure 9). BICUTIVOX data appear to be well-behaved, while the BICUVOX data are less-so. Using the activation energy for growth (83 kJ/mol) in equation 2 and the slope of the best fit line, one obtains a grain growth rate constant of 9.6 x 10^{-16} cm^2/sec. In this case, the y-intercept is 3.2 µm (interpreted as the starting grain size). If the best fit line is forced through the origin (starting size D_0=0 µm), then the rate constant increases to 16 x10^{-16} cm^2/sec. This rate constant is far below the estimated mobility of ionic species in a molten salt (1x10^{-8} cm^2/sec), but not far from the estimated mobility of species in the solid state (1x10^{-18}) cm^2/sec [18]. This suggests that the limiting mechanism for grain growth is the diffusion at the surface or near-surface of the platelets. For BICUVOX, the rate constant appears to be larger.

Peer-reviewed version available at Crystals 2018, 8, 170; doi:10.3390/cryst8040170

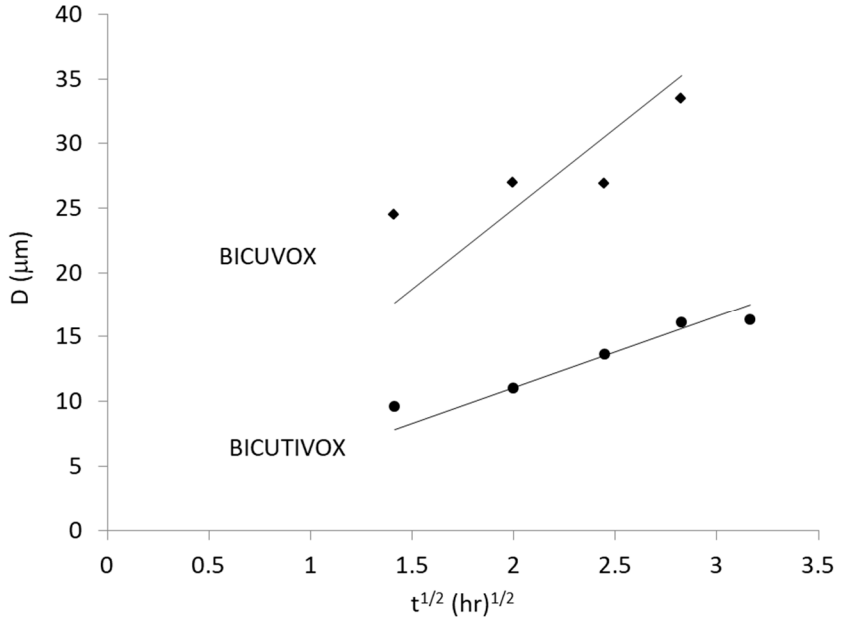

Figure 9. Platelet diameter versus the square root of time plots for BICUVOX and BICUTIVOX at an MSS process temperature of 650°C.

Inspection of the micrographs (Figures 2, 5 and 7) reveals differences between BICUVOX and BICUTIVOX. Most obvious is the size difference, but there is also a difference in particle form and edge angularity. BICUTIVOX particles can be described as having discoidal form with high circularity, and being sub-angular to well-rounded. In some cases, the particle takes on a multi-foil shape reminiscent of a Wulff construction [41-43]. Note the small penta-foil star on top of the larger, nearly round, multi-foil platelet in Figure 5(B). BICUVOX, on the other hand, can be described as discoidal with low circularity, and having angular to sub-rounded edges.

Figure 10 is a schematic which aids the description of the platelet growth and provides an explanation for their quasi-equilibrium, multi-foil shapes. The top row represents BICUTIVOX. The bottom row represents BICUVOX. In general, particles of Aurivillius type, bismuth layered structure compounds are expected to have atomically smooth *(00l)* faces, and atomically rough *(hk0)* faces [44], so high surface area sites nucleate along the propagating edge of a platelet (Fig. 10(B)). During Ostwald ripening, a kinetic restriction (surface diffusion) regulates the growth of the platelets but doesn't affect the 2D-nucleation rates for the ledge generation. In BICUTIVOX, nucleation of ledges (with fast kinetics) is distributed evenly about the perimeter of the crystallite, and so growth of the propagating edge happens evenly in all directions (Fig. 10(C)). The nucleation-growth process repeats itself as the particle grows (Fig. 10 (D-G)). For some particles, the process is interrupted at the nucleation stage; for others at the edge growth stage; for others somewhere in between (see especially Figure 5(B)). The lobes are more pronounced and more numerous in the higher temperature (700°C) material because the rate of nucleation is very high. In the case of BICUVOX, the mechanism of platelet growth is the same, except that there is a difference in the speed of edge propagation because the rate constant is higher (as seen in Figure 9). In BICUVOX, soon after the nucleation of a ledge site, the edge begins to grow around it as the cusp fills in due to capillary pressure. Because this growth step happens more rapidly than in

Peer-reviewed version available at Crystals 2018, 8, 170; doi:10.3390/cryst8040170

BICUTIVOX, the growth does not occur evenly in all directions; thus, the lack of circularity in BICUVOX platelets.

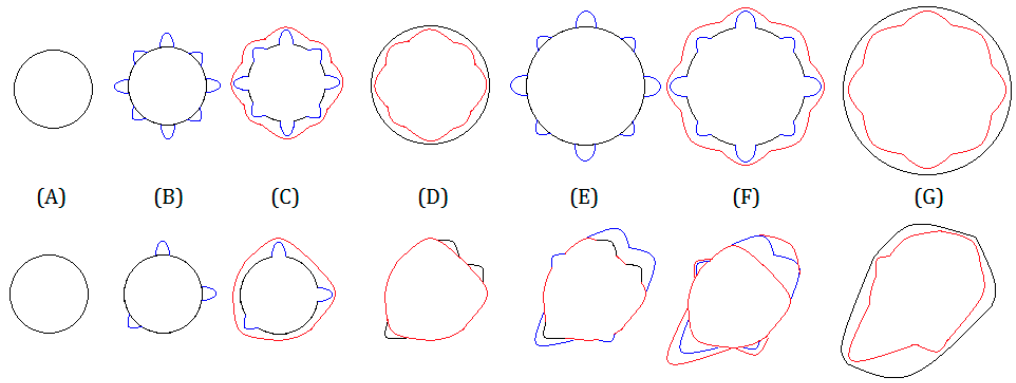

Figure 10. Schematic description of the kinetically limited growth mechanism undergone by BICUTIVOX (upper row) as compared to BICUVOX (bottom row). Different colors are used to indicate sequential layers of nucleation-growth.

The presence of the Ti^{4+} likely does not have a large effect on molten salt liquid diffusion rates, but does noticeably increase the activation energy and rate constant for growth. This is consistent with the known effect of solid solution, aleovalent impurities or substitutions acting as grain growth inhibitors in ceramics [39, 45]. In the presence of such solute ions, the activation energy for boundary migration is the sum of the vacancy migration, vacancy creation, impurity solution, and strain energy terms, but it is difficult to separate the relative contribution of each. Since doped BICUVOX contains significant oxygen vacancies and is a fast oxide ion conductor particularly in the *a-b* plane, it is conceivable that cations are the rate limiting diffusing species.

While evidence of edge roughness and lobes on MSS platelets can be found in previous published work [25,46,47], they generally do not appear as pronounced nor as regular multi-foil shapes like the BICUTIVOX material presented here. The closest example is found in Nd/V co-doped $Bi_4Ti_3O_{12}$ by Tang et al. [47]. To our knowledge, the shapes have not been explained or even addressed. The BICUTIVOX multi-foil and lobed platelets synthesized in this work are similar to Wulff construction polar plots of the anisotropic surface energies of crystal planes. They can be described as quasi-equilibrium shapes which result from the combination of both surface energy anisotropy and growth rate anisotropy, not just between *(00l)* and *(hk0)* planes, but also within the family of *(hk0)* planes. The growth rate anisotropy occurs when a particular crystal face affords easy atom/ion attachment and grows rapidly, and can result in shapes which exaggerate actual surface energy anisotropies [48]. Identification of the crystal planes within a multi-foil platelet, their correlation with edge lobes, and the role of aleovalent dopants are the subjects of future work.

5. Conclusions

The γ-phase of both BICUVOX and BICUTIVOX can be synthesized from simple metal oxides using a NaCl-KCl eutectic mix in a molten salt synthesis (MSS) process. The salt flux enhances grain growth with platelet habit, even with a process temperature 40°C below the eutectic temperature, indicating that whether solid or liquid, the salt increases the diffusion rates of ions and

facilitates anisotropic growth. The average size of platelets increases with process temperature as expected, but when the platelets grow to a diameter in excess of about 50 µm, significant fracture can be expected due to the rigors of post processing (washing/filtering), and therefore there is a practical limit to how large the platelets can be synthesized and recovered. Optimal results with respect to achieving high grain (*c*-axis or *(00l)*) orientation factors are achieved at 650°C, very near the salt eutectic temperature, for both compounds.

Titanium ion, Ti^{4+}, as a second, aleovalent substitution for V^{5+}, acts as a particle growth inhibitor during MSS. The activation energy for platelet growth of BICUTIVOX in the molten salt is 83 kJ/mol, which is consistent with MSS values reported in the literature for other simple and complex perovskites. The (growth) reaction rate constant at 650°C is 10 to 16 x 10^{-16} cm^2/sec, indicating that the limiting mechanism for platelet growth is the (near) surface reaction and diffusion. Due to the significant difference in 2D nucleation and edge propagation rates during Ostwald ripening, BICUTIVOX shows a tendency for multi-foil platelet shapes with pronounced lobes extending from platelet edges. Faster volume and/or surface diffusion in BICUVOX allows higher overall growth rate and causes the platelet shape to be non-circular and more angular. Future interest may lie in producing lobed platelets with higher surface area to take advantage of the high oxide ion mobility in the *(00l)* (*a-b* crystal) plane and functionality of the *(hk0)* surfaces in BICUTIVOX.

Acknowledgments: This research was funded by the National Science Foundation (Materials World Network, Division of Materials Research grant # 1108466). The authors also acknowledge the assistance of Mr. Riley Reproglie with image analysis and particle size measurement.

Author Contributions: Kevin Ring performed the synthesis and characterization of the samples, and wrote the first draft of the manuscript. Paul Fuierer conceived the original idea, managed the overall project, and wrote and edited the final manuscript.

Conflicts of Interest: The authors declare no conflict of interest.

References

1. Abraham, K; Debreuille, M.; Mairesse, G.; Nowogrocki. G.. Phase transitions and ionic conductivity in $Bi_4V_2O_{11}$ an oxide with a layered structure. *Solid State Ionics* **1988**, *28-30*, 529-532.
2. Abraham, F.; Boivin, J.; Mairesse, G.; Nowogrocki, G. The BIMEVOX Series: A New Family of High Performance Oxide Ion Conductors. *Solid State Ionics* **1990**, *40-41*, 934-937.
3. Yaremchenko, A; Avdeev,M.; Kharton, K.; Kovalevsky, A.; Naumovich, E.; Marques, F. Structure and electronic conductivity of $Bi_{2-x}La_xV_{0.9}Cu_{0.1}O_{5.5-\delta}$. *Mat. Chem. & Phys.* **2002**, 77 Issue 2, 552-558.
4. Kurek, P.; Dygas, J.; Breiter, M. Impedance measurements on single crystals of the oxygen ion conductor BICUVOX. *J.of Electroanalytical Chem.* **1994**, 378, Issue 1-2, 77-83.
5. Goodenough, J. Oxide-Ion Electrolytes, a review. *Ann. Rev. of Mat. Res.* **2003**, 33, 91-128.
6. Kendall, K.; Navas, C.; Thomas, J.; Loye, H. Recent Developments in Oxide Ion Conductors: Aurivillius Phases. *Chem. of Mat.* **1996**, 8, 642-649.
7. Cho, H.; Sakai, G.; Shimanoe, K.; Yamazoe, N. Preparation of BiMeVOx (Me=Cu, Ti, Zr, Nb, Ta) compounds as solid electrolyte and behavior of their oxygen concentration cells. *Sensors and Actuators B: Chemical* **2005**, 109, Issue 2, 307-314.
8. Kida, T.; Minami, T.; Kishi, S.; Yuasa, M.; Shimanoe, K.; Yamazoe, N. Planar-type BiCuVOx solid electrolyte sensor for the detection of volatile organic compounds. *Sensors and Actuators B: Chem.* **2009**, 137,147-153.
9. Kida, T.; Harano, H.; Minami, T.; Kishi, S.; Morinaga, N.; Yamazoe, N.; Shimanoe, K. Control of electrode reactions in a mixed- potential-type gas sensor based on a BiCuVOx solid electrolyte. *J. Phys. Chem. C* **2010**, 114, 15141-48.
10. Patil, B.; Sharma, S.; Mohanta, H.; Roy, B. BINIVOX catalyst for hydrogen production from ethanol by low temperature steam reforming (LTSR). *J. Chem. Sci.* **2017**, 129 [11] 1741-1746, doi.org/10.1007/s12039-017-1388-x.
11. Fuierer, P.; Maier, R.; Roder-Roith; U.; Moos, R. Processing Issues Related to the Bi-dimensional Ionic Conductivity of BIMEVOX Ceramics. *J. Mater. Sci.* **2011**, 46 [16] 5447-53.
12. Sant, C.; Contour, J. Pulsed laser deposition of $Bi_4Cu_2xV_{2(1-x)}O_{11}$ thin films. *J. Cryst. Growth* ***1995***, 153, 63-67.
13. Muller, C.; Chateigner, D.; Anne, M.; Bacmann, M.; Fouletier, J.; Rango, P. Pressure and magnetic field effects on the crystallographic texture and electrical conductivity of the compound. *J. Phys. D: Appl. Phys.* **1996**, 29, 3106-3111.
14. Fuierer, P.; Nichtawitz, A. Electric Field Assisted Hot Forging of Bismuth Titanate. *Proc. Ninth IEEE Int. Symp. Appl. Ferroelectr*. **1994**, 9, 126-129.
15. Fuierer, P.; Newnham, R. *J. Amer. Ceram. Soc.* **1991**, 74, 2876-2881.
16. Fuierer, P.; Maier, M.; Exner, J.; Moos, R. Anisotropy and thermal stability of hot-forged BICUTIVOX oxygen ion conducting ceramics. *J. Eur. Ceram. Soc.* **2014**, 34, 943-951.
17. Shantha, K.; Varma, K. Fabrication and characterization of grain-oriented bismuth vanadate ceramics. *Mater. Res. Bull.* **1997**, 32, 1581-91.
18. Seth, V.; Schulze, W. Grain-Oriented Fabrication of Bismuth Titanate Ceramics and Its Electrical Properties. *IEEE Transactions on Ultrasonics, Ferroelectrics, and Frequency Control* **1989**, 36, Issue 1, 41-42.
19. Watanabe, H.; Kimura, T.; Yamaguchi, T. Particle Orientation During Tape Casting in the Fabrication of Grain-Oriented Bismuth Titanate. *J. Amer. Ceram. Soc.* **1989**, 72, Issue 2, 289-293.
20. Horn, J.; Zhang, S.; Selvaraj, U.; Messing, G.; Trolier, S. Templated Grain Growth of Textured Bismuth Titanate. *J. Amer. Ceram. Soc. 1999,* 82, Issue 4, 921-926.
21. Yilmaz, H.; Messing, G.; Trolier, S. (Reactive) Templated Grain Growth of Textured Sodium Bismuth Titanate ($Na_{0.5}Bi_{0.5}TiO_3$-$BaTiO_3$) Ceramics-I Processing. *Journal of Electroceramics*, 2003, 11, 207-215.
22. West, D.; Payne, D. Reactive-Templated Grain Growth of $Bi_{0.5}(Na,K)_{0.5}TiO_3$: Effects of Formulation on Texture Development. *J. Amer. Ceram. Soc* **2003**, 86, Issue 7, 1132-1137
23. Kimura, T.; Yoshida, Y. Origin of Texture Development in Barium Bismuth Titanate Prepared by the Templated Grain Growth Method. *J. Amer. Ceram. Soc* **2006**, 89, Issue 3, 869-874.
24. Arendt, R.; Rosolowski, J.; Szymaszek J. Lead zirconate titanate ceramics from molten salt solvent synthesized powders. *Materials Research Bulletin* **1979**, 15, Issue 5, 703-709.
25. Kimura, T. & Yamaguchi, T. Fused Salt Synthesis of $Bi_4Ti_3O_{12}$. *Ceramics International* **1983**, 9, No.1, 13-17 ISSN 0272-8842.

26. Li, Z.; Zhang, X.; Hou, J.; Zhou, K. Molten salt synthesis of anisometric $Sr_3Ti_2O_7$ particles. *J. Cryst. Growth* **2007**, 305, 265-270.
27. Kimura, T. Chapt. 4 Molten Salt Synthesis of Ceramic Powders. In *Advances in Ceramics - Synthesis and Characterization, Processing and Specific Applications*, Editor Sikalidis, C.; INTECH, Croatia, 2011; pp. 75-100, ISBN 978-953-307-505-1.
28. Liu, X.; Fechler, N.; Antonietti, M. Salt melt synthesis of ceramics, semiconductors and carbon nanostructures, *Chem. Soc. Rev* **2013**, 42, 8237-8265.
29. Preethi, G.; Ninan, A.; Kumar, K.; Balan, R.; Nagaswarupa, H. Molten Salt Synthesis of Nanocrystalline $ZnFe_2O_4$ and Its Photocatalytic Dye Degradation Studies. Materials Today: Proceedings **2017**, 4, 11816-11819.
30. Kang, M.; Kim, D.; Hwang, N. Ostwald ripening kinetics of angular grains dispersed in a liquid phase by two dimensional nucleation and abnormal grain growth. *J. Eur. Ceram. Soc.* **2002**, 22, Issue 5, 603-612.
31. Roy, B.; Fuierer, P. Molten Salt Synthesis of $Bi_4(V_{0.85}Co_{0.15})_2O_{11-\delta}$ (BICOVOX) Ceramic Powders. *J. Amer. Ceram. Soc*. **2009**, 92 [2] 520-523.
32. Sangster, J.; Pelton, A. Phase Diagrams and Thermodynamic Properties of the 70 Binary Alkali Halide Systems Having Common Ions. *J. Phys. and Chem. Ref. Data* **1987**, 16, 509.
33. Powder Diffraction File #01-070-9191, Bismuth Vanadium Copper Oxide, International Center for Diffraction Data.
34. Inoue, M.; Hirasawa, I. The relationship between crystal morphology and XRD peak intensity on $CaSO_4{\cdot}2H_2O$. *J. Cryst. Growth* **2013**, 380, 169-175.
35. Roy, B.; Scott P.; Ahrenkiel, Y.; Fuierer, P. Controlling the Size and Morphology of TiO_2 Powder by Molten and Solid Salt Synthesis. *J. Am. Ceram. Soc.* **2008**, 91 [8], 2455–2463 (2008)
36. Betz, W.; Webb, H. Plane Geometry, Book V. Regular Polygons and Circles, Ginn & Co., **1921**; p. 321.
37. Lotgering, F. Topotactical Reaction with Ferrimagnetic Oxides Having Hexagonal Structures. *J. of Inorganic and Nuclear Chem.* **1959**, 9, Issue 2, 113-123.
38. Yoon, K.; Yong, S.; Kang, D. Review: Molten Salt synthesis of lead-based relaxors. *J. Mat Sci.* **1998**, 33, 2977-2984.
39. Kapadia, L. The Mechanism of Grain Growth in Ceramics. NASA Report **1973**, pp. 6-34.
40. Gu, Y.; Huang, J.; Li, L.; Zhang, K.; Wang, X; Li, Q.; Tan, X.; Xu, H. Molten salt synthesis of anisotropy $BaBi_4Ti_4O_{15}$ powders in K_2SO_4-Na_2SO_4 flux. *Mat. Sci. Forum* **2011**, 687, 333-338.
41. Wulff, G. Zur Frage der Geschwindigkeit des Wachsthums und der Auflösung der Krystallflächen. *Z. Kristallogr.* **1901**, 34, 449-530.
42. Herring, C. Some Theorems on the Free Energies of Crystal Surfaces. *Phys Rev.* **1951**, 82 [1], 87-93.
43. Kang, S. Ch. 15 Grain Shape and Grain Growth in a Liquid Matrix. In *Sintering*, Elsevier, Great Britain, **2005**, p.218.
44. Kimura, T.; Tani, T. Chapt 15, Processing and Properties of Textured Bismuth Layer-Structured Ferroelectrics. In *Lead Free Piezoelectrics*, Editors Priya, S.; Nahm, S., Springer-Verlag: New York, **2012**; p. 465, ISBN 978-1-4419-9598-8.
45. Hollenberg, G.; Gordon, R. Origin of Anomalously High Activation Energies in Sintering and Creep of Impure Refractory. *J. Am Ceram Soc* **1973**, 56 [2], 109-110.
46. Afanasiev, P. Preparation of Mixed Phosphates in Molten Alkali Metal Nitrates, *Chem. Mater.* **1999**, 11, 1999-2007.
47. Tang, Q.,; Yan-Mei, Z.; Kan, Z.; Wang, P.; Yao-Gang Li, W.; Zhang, G. Nd/V Co-Doped $Bi_4Ti_3O_{12}$ Powder Prepared By Molten Salt Synthesis. *J. Am. Ceram. Soc.* **2007**, 90 [10] 3353–3356.
48. Chiang, Y.; Birnie, D.; Kingery, W. Chapter 5, Microstructure. In *Physical Ceramics*; J. Wiley & Sons: New York, 1997; p. 354, ISBN 0-471-59873-9.